\




# Characteristics of temperature fluctuation in two-dimensional turbulent Rayleigh-Bénard convection

Ming-Wei Fang(方明卫), Jian-Chao He(何建超), Zhan-Chao Hu(胡战超), and Yun Bao(包芸)†

**Citation:**Chin. Phys. B, 2022, 31 (**1**): 014701. DOI: 10.1088/1674-1056/ac012f
Journal homepage: http://cpb.iphy.ac.cn; http://iopscience.iop.org/cpb

**What follows is a list of articles you may be interested in**

---

## Effects of Prandtl number in two-dimensional turbulent convection

Jian-Chao He(何建超), Ming-Wei Fang(方明卫), Zhen-Yuan Gao(高振源), Shi-Di Huang(黄仕迪), and Yun Bao(包芸)

Chin. Phys. B, 2021, 30 (**9**): 094701. DOI: 10.1088/1674-1056/ac0781

## Molecular-dynamics investigation of the simple droplet critical wetting behavior at a stripe pillar edge defect

Xiaolong Liu(刘小龙), Chengyun Hong(洪成允), Yong Ding(丁勇), Xuepeng Liu(刘雪朋), Jianxi Yao(姚建曦), Songyuan Dai(戴松元)

Chin. Phys. B, 2019, 28 (**1**): 014703. DOI: 10.1088/1674-1056/28/1/014703

## Bifurcation phenomena and control for magnetohydrodynamic flows in a smooth expanded channel

G. C. Layek, Mani Shankar Mandal, H. A. Khalaf

Chin. Phys. B, 2014, 23 (**11**): 114701. DOI: 10.1088/1674-1056/23/11/114701

## Cross-diffusive effects on the onset of the double-diffusive convection in a horizontal saturated porous fluid layer heated and salted from above

Rajib Basu, G. C. Layek

Chin. Phys. B, 2013, 22 (**5**): 054702. DOI: 10.1088/1674-1056/22/5/054702

## Imperfect pitchfork bifurcation in asymmetric two-compartment granular gas

Zhang Yin, Li Yin-Chang, Liu Rui, Cui Fei-Fei, Pierre Evesque, Hou Mei-Ying

Chin. Phys. B, 2013, 22 (**5**): 054701. DOI: 10.1088/1674-1056/22/5/054701

---

# Characteristics of temperature fluctuation in two-dimensional turbulent Rayleigh–Bénard convection

Ming-Wei Fang(方明卫), Jian-Chao He(何建超), Zhan-Chao Hu(胡战超), and Yun Bao(包芸)†

*School of Aeronautics and Astronautics, Sun Yat-sen University, Guangzhou* 510275, *China*

(Received 11 March 2021; revised manuscript received 11 May 2021; accepted manuscript online 14 May 2021)

We study the characteristics of temperature fluctuation in two-dimensional turbulent Rayleigh–Bénard convection in a square cavity by direct numerical simulations. The Rayleigh number range is $1\times10^8 \le Ra \le 1\times10^{13}$, and the Prandtl number is selected as $Pr = 0.7$ and $Pr = 4.3$. It is found that the temperature fluctuation profiles with respect to $Ra$ exhibit two different distribution patterns. In the thermal boundary layer, the normalized fluctuation $\theta_{\rm rms}/\theta_{\rm rms,max}$ is independent of $Ra$ and a power law relation is identified, *i.e.*, $\theta_{\rm rms}/\theta_{\rm rms,max} \sim (z/\delta)^{0.99\pm0.01}$, where $z/\delta$ is a dimensionless distance to the boundary ($\delta$ is the thickness of thermal boundary layer). Out of the boundary layer, when $Ra \le 5\times10^9$, the profiles of $\theta_{\rm rms}/\theta_{\rm rms,max}$ descend, then ascend, and finally drop dramatically as $z/\delta$ increases. While for $Ra \ge 1\times10^{10}$, the profiles continuously decrease and finally overlap with each other. The two different characteristics of temperature fluctuations are closely related to the formation of stable large-scale circulations and corner rolls. Besides, there is a critical value of $Ra$ indicating the transition, beyond which the fluctuation $\langle\theta_{\rm rms}\rangle_V$ has a power law dependence on $Ra$, given by $\langle\theta_{\rm rms}\rangle_V \sim Ra^{-0.14\pm0.01}$.

**Keywords:** Rayleigh–Bénard, temperature fluctuation, distribution patterns, critical value

**PACS:** 47.27.te **DOI:** 10.1088/1674-1056/ac012f

## 1. Introduction

Turbulent thermal convection occurs ubiquitously in both nature and engineering applications. Turbulent Rayleigh–Bénard convection (RBC), a closed fluid layer thermostatically heated from the bottom and cooled from the top, has chronically been used to study thermally-driven turbulence.[1–4] The enclosed working fluid forms convective motion through the buoyancy force produced by the temperature difference between the bottom and the top plates of a convection cell of height $H$.

Turbulent RBC is controlled primarily by two dimensionless parameters, namely the Rayleigh number and the Prandtl number, defined as $Ra = \alpha g\Delta\theta H^3/(\kappa\upsilon)$ and $Pr = \upsilon/\kappa$, respectively, where $\Delta\theta$ is the temperature difference, $g = 9.81$ m/s$^2$ is the gravitational acceleration, and $\alpha$, $\upsilon$, and $\kappa$ are, respectively, the thermal expansion coefficient, the kinematic viscosity, and the thermal diffusivity. Apart from $H$, the geometry of the convection cell also influences turbulent RBC. Therefore, in classical cubic and cylindrical cells, the aspect ratio also becomes a crucial parameter.

A core task in the study of turbulent RBC is to understand the heat transport in turbulent flows. In general, the Nusselt number, defined as

$$Nu = \langle\sqrt{Ra\cdot Pr}\cdot v\theta\rangle_{V,t} - \left\langle\frac{\partial\theta}{\partial z}\right\rangle_{V,t}, \tag{1}$$

where $\langle\cdots\rangle_{V,t}$ represents the average over space and time. It is usually calculated to reflect the strength of heat transport. In 2000, Grossmann and Lohse put forward the so-called GL theory[5–7] to predict $Nu$ according to $Ra$ and $Pr$ by decomposing the energy dissipation. There are two kinds of characteristic structures that are related to heat transport. One is the large-scale circulation, also known as 'wind' of the bulk fluid,[8–10] and the other kind of structure is a cluster of thermal plumes[11–13] that erupts intermittently from the thermal boundary layer. Previous researches have revealed that the heat transport is governed primarily by thermal plumes.[14–18] Moreover, the intensity of thermal plumes can be measured by the amplitude of local temperature fluctuations. In other words, the local temperature fluctuations and heat transport are closely linked to each other. According to the definition, the amplitude of local temperature fluctuations is measured at each specific point. To simplify the study, fortunately, it is convenient to examine the profile of the local temperature fluctuations, defined as

$$\theta_{\rm rms}(z) = \langle\langle(\theta - \langle\theta\rangle)^2\rangle^{1/2}\rangle_x, \tag{2}$$

where $\langle\cdots\rangle_x$ represents the average over horizontal direction and the subscript $t$ of time average is omitted. One can extract the information about flow state, plume distribution, and heat transport from $\theta_{\rm rms}(z)$. Therefore, $\theta_{\rm rms}(z)$ has been studied frequently in previous work.

According to the Castaing *et al.*'s theory,[19] Adrian identified two new profiles, termed as $\lambda$–I and $\lambda$–II models.[20] Recently, looking into the so-called mixing zone, the similarities in $\theta_{\rm rms}(z)$ between the thin disk and the cylinder cells have been revealed.[21,22] He and Xia[23] investigated $\theta_{\rm rms}(z)$ in the shear-dominated zone and the plume-dominated mixing zone

†Corresponding author. E-mail: stsby@mail.sysu.edu.cn

© 2022 Chinese Physical Society and IOP Publishing Ltd 

in a elongated cubic cell. They that the reported $\theta_{\rm rms}(z)$ is a power-law function of $z$ in the former region, and a logarithmic function in the latter region. Afterward, such a power-law has also been identified in non-elongated cells with different geometries.[24,25] There are also some experimental researches only focusing on $\theta_{\rm rms}$ in the cell center. The $Ra$-dependent $\theta_{\rm rms}$ shows the diverse traits in different geometries.[26–31] For example, Huang and Xia[32] discovered that $Ra$-scaling of $\theta_{\rm rms}$ increases with the aspect ratio.

In this paper, we present a direct numerical study on the characteristics of $\theta_{\rm rms}(z)$ in a two-dimensional (2D) turbulent RBC. Two different values of $Pr$ are considered, *i.e.*, 0.7 and 4.3. For both of them, the same range of $Ra$ is assigned: $1\times10^8 \le Ra \le 1\times10^{13}$. The rest of this paper is arranged as follows. In Section 2, we elaborate the governing equations and numerical methods. In Sections 3 and 4, characteristics of local temperature fluctuations and global temperature field for $Pr = 4.3$ and $Pr = 0.7$ are presented and discussed, respectively. The $Ra$-dependence of the mean temperature fluctuation is discussed in in Section 5. Our findings are summarized and also some conclusions are drawn in Section 6 finally.

## 2. Model and numerical methods

We perform direct numerical simulations (DNS) of 2D turbulent RBC in a square cavity. The non-dimensional governing equations under the Oberbeck–Boussinesq approximation are given by

$$\begin{cases} \nabla\cdot\boldsymbol{u}=0, \\ \dfrac{\partial\boldsymbol{u}}{\partial t}+(\boldsymbol{u}\cdot\nabla)\,\boldsymbol{u}=-\nabla p+\dfrac{1}{\sqrt{Ra/Pr}}\nabla^2\boldsymbol{u}+\theta\boldsymbol{k}, \\ \dfrac{\partial\theta}{\partial t}+(\boldsymbol{u}\cdot\nabla)\,\theta=\dfrac{1}{\sqrt{Ra\cdot Pr}}\nabla^2\theta, \end{cases} \tag{3}$$

where $\boldsymbol{u}$, $\theta$, and $p$ are respectively the non-dimensional velocity, temperature, and pressure, $\boldsymbol{k}$ is the vertical unit vector. $Ra$ and $Pr$ are the control parameters of the system as mentioned previously. Impermeable and no-slip boundary conditions are imposed on all walls. For temperature, the two vertical sidewalls are adiabatic, while the top and bottom plates are fixed at $\theta_{\rm t}=-0.5$ and $\theta_{\rm b}=0.5$, respectively. Thus, the dimensionless temperature difference between the two horizontal plates is $\Delta=\theta_{\rm b}-\theta_{\rm t}=1$. Governing equations are solved by the parallel direct method (PDM) of DNS (or PDM–DNS)[33,34] with using staggered grids.

All simulations are carried out on the Tianhe-2 supercomputer. The parameters of all cases are summarized in Fig. 1(a). Figure 1(b) presents a sketch of the time-averaged temperature fluctuation field, in which the thick black solid line (the central line) is the sampling region analyzed in this paper. In view of its symmetry, we choose the zone from the bottom to the center of the sampling region.

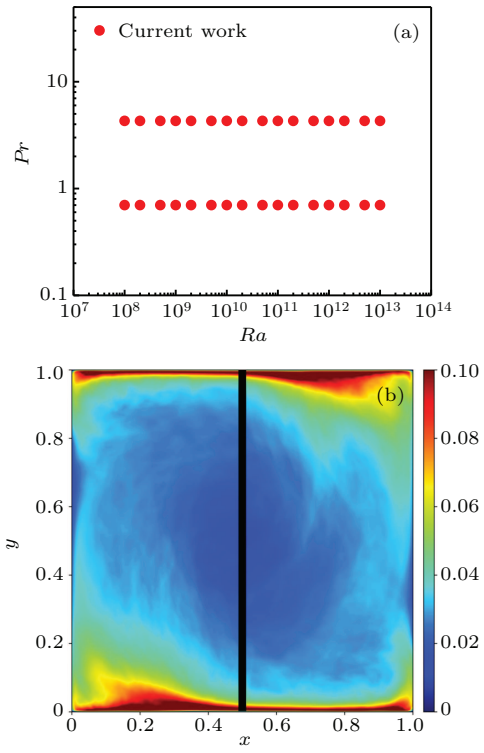



**Fig. 1.** (a) Simulated cases scattered in ($Ra$, $Pr$) plane. (b) Contour plot of time-averaged temperature fluctuation field, with solid line denoting sampling region.

**Table 1.** Parameters of conducted DNS of 2D RBC.

| $Pr$ | $Ra$ | $N_x\times N_y$ | $Nt_{\rm avg}$ | $Nu$ | $Re$ |
|---|---|---|---|---|---|
| 0.7 | $1\times10^8$ | $512\times576$ | 1000 | $2.52\times10^1$ | $6.77\times10^3$ |
| 0.7 | $2\times10^8$ | $512\times576$ | 1000 | $3.13\times10^1$ | $9.74\times10^3$ |
| 0.7 | $5\times10^8$ | $1024\times1152$ | 1000 | $4.21\times10^1$ | $1.60\times10^4$ |
| 0.7 | $1\times10^9$ | $1024\times1152$ | 400 | $5.05\times10^1$ | $1.57\times10^4$ |
| 0.7 | $2\times10^9$ | $1024\times1152$ | 400 | $5.98\times10^1$ | $2.33\times10^4$ |
| 0.7 | $5\times10^9$ | $1024\times1152$ | 400 | $7.83\times10^1$ | $3.68\times10^4$ |
| 0.7 | $1\times10^{10}$ | $1536\times1728$ | 400 | $9.53\times10^1$ | $5.65\times10^4$ |
| 0.7 | $2\times10^{10}$ | $2048\times2304$ | 400 | $1.18\times10^2$ | $8.19\times10^4$ |
| 0.7 | $5\times10^{10}$ | $2048\times2304$ | 400 | $1.58\times10^2$ | $1.45\times10^5$ |
| 0.7 | $1\times10^{11}$ | $2048\times2304$ | 400 | $1.98\times10^2$ | $2.11\times10^5$ |
| 0.7 | $2\times10^{11}$ | $2560\times2880$ | 200 | $2.43\times10^2$ | $2.81\times10^5$ |
| 0.7 | $5\times10^{11}$ | $2560\times2880$ | 200 | $3.26\times10^2$ | $4.64\times10^5$ |
| 0.7 | $1\times10^{12}$ | $4096\times4608$ | 400 | $4.00\times10^2$ | $6.43\times10^5$ |
| 0.7 | $2\times10^{12}$ | $4096\times4608$ | 300 | $5.02\times10^2$ | $9.17\times10^5$ |
| 0.7 | $5\times10^{12}$ | $5120\times5760$ | 200 | $6.67\times10^2$ | $1.42\times10^6$ |
| 0.7 | $1\times10^{13}$ | $5120\times5760$ | 100 | $8.40\times10^2$ | $2.04\times10^6$ |
| 4.3 | $1\times10^8$ | $512\times576$ | 250 | $2.57\times10^1$ | $1.21\times10^3$ |
| 4.3 | $2\times10^8$ | $512\times576$ | 700 | $3.14\times10^1$ | $1.92\times10^3$ |
| 4.3 | $5\times10^8$ | $512\times576$ | 400 | $4.13\times10^1$ | $3.38\times10^3$ |
| 4.3 | $1\times10^9$ | $1024\times1152$ | 400 | $5.08\times10^1$ | $4.96\times10^3$ |
| 4.3 | $2\times10^9$ | $1024\times1152$ | 400 | $6.32\times10^1$ | $7.23\times10^3$ |
| 4.3 | $5\times10^9$ | $1024\times1152$ | 400 | $8.37\times10^1$ | $1.20\times10^4$ |
| 4.3 | $1\times10^{10}$ | $1024\times1152$ | 800 | $1.02\times10^2$ | $1.28\times10^4$ |
| 4.3 | $2\times10^{10}$ | $1536\times1728$ | 800 | $1.24\times10^2$ | $1.83\times10^4$ |
| 4.3 | $5\times10^{10}$ | $2048\times2304$ | 600 | $1.60\times10^2$ | $2.91\times10^4$ |
| 4.3 | $1\times10^{11}$ | $2560\times2880$ | 500 | $1.94\times10^2$ | $4.51\times10^4$ |
| 4.3 | $2\times10^{11}$ | $2560\times2880$ | 400 | $2.36\times10^2$ | $6.74\times10^4$ |
| 4.3 | $5\times10^{11}$ | $2560\times2880$ | 400 | $3.13\times10^2$ | $1.25\times10^5$ |
| 4.3 | $1\times10^{12}$ | $3072\times3456$ | 600 | $3.93\times10^2$ | $1.39\times10^5$ |
| 4.3 | $2\times10^{12}$ | $3840\times4320$ | 600 | $4.88\times10^2$ | $2.06\times10^5$ |
| 4.3 | $5\times10^{12}$ | $4096\times4608$ | 250 | $6.52\times10^2$ | $3.61\times10^5$ |
| 4.3 | $1\times10^{13}$ | $5120\times5760$ | 100 | $8.08\times10^2$ | $4.73\times10^5$ |

Table 1 shows the detailed parameters of the simulation of RBC. The number of nodes in each direction of the computational mesh is $N_x \times N_y \cdot Nt_{\rm avg}$ is the number of dimensionless time ($\tau$) units used for the statistical averaging. *Nu* and *Re* numbers are the statistical non-dimensional heat transfer *Nu* number and the small scale Reynolds number, respectively.

## 3. Results and discussion for $Pr = 4.3$

### 3.1. Mean temperature profile and probability density distribution of temperature

The thermal plumes, emitted intermittently from the conducting plates, play an important role in heat transfer of turbulent thermal convection. The plume is the only thermal structure in the system, and its temperature characteristics are analyzed through temperature statistics. We present the statistical results of temperature at different values of *Ra*.

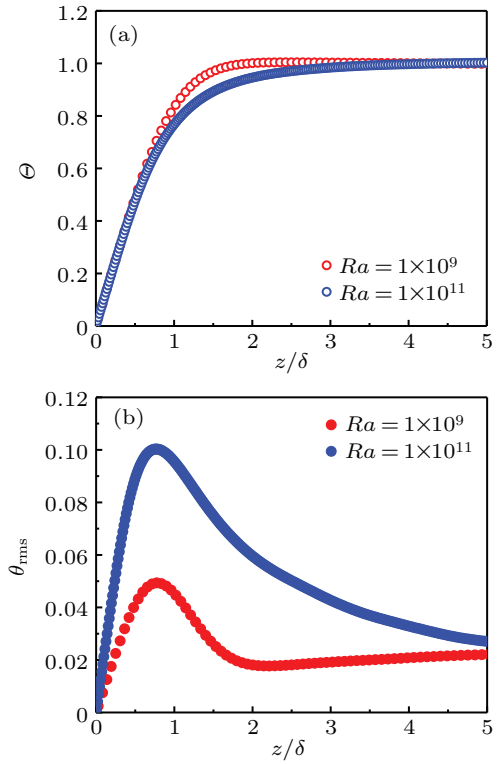



**Fig. 2.** (a) Profiles of normalized mean temperature $\Theta$ at two different values of *Ra* for $Pr = 4.3$. (b) Corresponding temperature fluctuation $\theta_{\rm rms}$ profiles.

Figure 2 shows the calculated mean temperature profile $\Theta$ (open circles) and temperature fluctuation profile $\theta_{\rm rms}$ (solid circles) each as a function of normalized distance $z/\delta$ from the lower plate along central axis region of flow space for two typical *Ra* values, with $Pr = 4.3$ fixed. Here $\delta$ is the thickness of the thermal boundary layer (BL) defined by the slope method.[35] The mean temperature $\Theta$ is normalized and defined as $\Theta = [\theta_{\rm bot} - \langle\theta(x,z)\rangle_x]/\theta_{\rm bot}$, where $\theta_{\rm bot}$ and $\langle\cdots\rangle_x$ are respectively the temperature of the bottom plate and the average over horizontal direction. In Fig. 2(a), the mean temperature profiles overlap each other and rise rapidly inside the thermal BL. When $z/\delta > 1$, the mean temperature gradually approaches to the central temperature. At $Ra = 1\times10^{11}$, it tends to the central temperature more slowly. After three thermal BLs, the temperature profiles overlap again and reach the core temperature. Note also from Fig. 2(b) that the temperature fluctuation profiles show significantly different characteristics. The temperature fluctuation rises fast and reaches a maximum value, then always decays for $Ra = 1\times10^{11}$. While for $Ra = 1\times10^{9}$, the temperature fluctuation change is relatively small. The overall temperature fluctuation first increases, then decreases, and finally rises slowly. The temperature fluctuation profiles of two *Ra* numbers reach their corresponding maximum values near the thermal boundary layers.

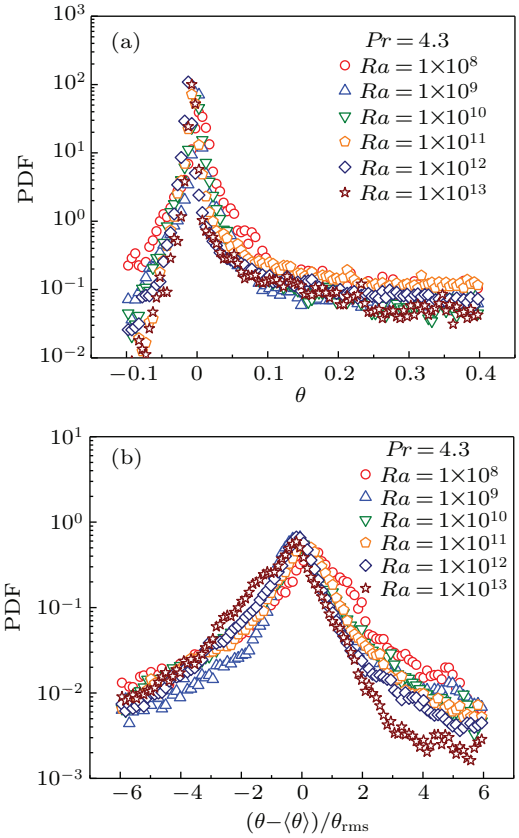



**Fig. 3.** PDF of local temperature and normalized temperature fluctuations for several values of *Ra*.

Temperature probability density distribution (PDF) represents the proportion of the temperature distribution in the region, where PDF stands for probability density distribution. Figure 3(a) shows PDF of the temperature in the central axis region (from the bottom to the center) for different values of *Ra*. It is seen that the PDFs from five different values of *Ra* are very similar, and can be well described as exponential functions. The bulk temperature s skews significantly towards higher temperature. It is seen that as *Ra* increases, the probability of occurrence of lower temperature at the left tail decreases, while the phenomenon does not exist for higher temperature at the right tail. By measuring the temperatures of six different positions on the central axis, Zhou and Xia[35] found

that the PDF of temperature in the boundary layer presents a nearly Gaussian shape, and the PDFs of other positions are different from each other.

Figure 3(b) shows the plots of the corresponding PDFs of the normalized temperature fluctuations obtained at different values of *Ra*. It is seen that all the PDFs exhibit almost an exponential shape of symmetry. While, in previous experiments it was found that the normalized temperature fluctuation in the center of the cell can be well described by a stretched exponential function.[31,32,36,37] The right tail shifts slightly downward high *Ra*, indicating that the probability of larger temperature fluctuation decreases. The PDF form of temperature fluctuation has apparent distinctions for different flowing states.

### 3.2. Local temperature fluctuations

Plume, as the most prominent thermal structure in RB system, is closely related to the temperature fluctuation of the system, and it possesses its own characteristics and motion mode. The local temperature fluctuation is an important indication for plume spatial distribution. Figure 4 shows a log-log plot of temperature fluctuation $\theta_{\rm rms}$ as a function of the normalized distance $z/\delta$ for various values of *Ra*.

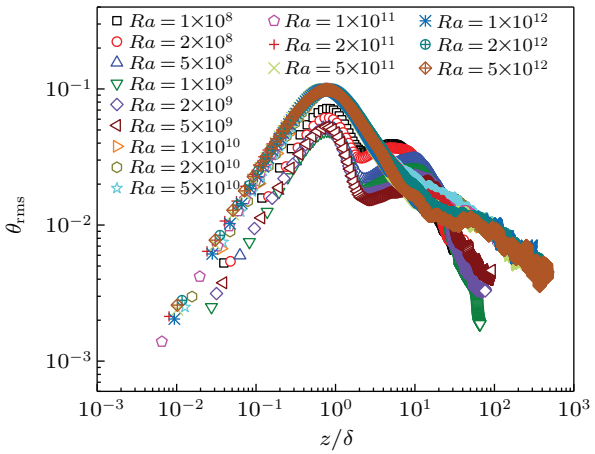



**Fig. 4.** Profiles of measured temperature fluctuation $\theta_{\rm rms}$ corresponding to half the black solid line region in Fig. 1(b) (from bottom plate to center), and at various values of *Ra* from $1.0\times10^8$ to $1.0\times10^{13}$.

Figure 2 shows that the temperature fluctuation profile increases linearly in the boundary layer, and then decays away from the plate. It can be seen from Fig. 4 that there are two distribution patterns. Under $1\times10^8 \le Ra \le 5\times10^9$, the temperature fluctuation profiles have two peaks at about $z/\delta = 1$ and $z/\delta = 10$ respectively. The two peaks of the temperature fluctuation profiles decrease with *Ra* increasing. It is seen from this figure that for *Ra* greater than $5\times10^9$, the temperature fluctuation profiles all collapse into a single curve. The $\theta_{\rm rms}$ profiles rise first and then decrease when leaving from the bottom plate, reaching a peak at about $z/\delta = 1$.

The comparison between the two types of $\theta_{\rm rms}$ profiles of $Ra \le 5\times10^9$ and $Ra \ge 1\times10^{10}$ shows that the $\theta_{\rm rms}$ profiles are overall significantly larger for $Ra \ge 1\times10^{10}$. This means that system flow status and plume distribution are obviously different.

Figure 5 shows the plots of the normalized temperature fluctuation $\theta_{\rm rms}/\theta_{\rm rms,max}$ *versus* $z/\delta$ and in these figures the values of $\theta_{\rm rms}$ were measured in the thin disk from Wang *et al.*[21,22] and in the cylinder from Wang *et al.*,[22] respectively, where $\theta_{\rm rms,max}$ represents the maximum value of $\theta_{\rm rms}$. It shows clearly that all profiles of the normalized temperature fluctuation $\theta_{\rm rms}/\theta_{\rm rms,max}$ for different values of *Ra* collapse into a single curve quite well inside the thermal BL, which implies that in the $\theta_{\rm rms}/\theta_{\rm rms,max}$ profiles there exists a self-similarity or independence of *Ra*. Beyond the boundary layer, for different values of *Ra*, $\theta_{\rm rms}/\theta_{\rm rms,max}$ profiles take on different distribution characteristics. In the range of $Ra < 1\times10^{10}$, when moving away from the BL, temperature fluctuation profiles $\theta_{\rm rms}/\theta_{\rm rms,max}$ decrease with $z/\delta$ increasing, then moderately increase in the region $1 \le z/\delta \le 10$, and finally drop dramatically. With $z/\delta$ varying from 1 to 10, the ascending slope gradually decreases with *Ra* increasing. The appearance may be caused by corner rolls' motion. For $Ra \ge 1\times10^{10}$, the $\theta_{\rm rms}/\theta_{\rm rms,max}$ profiles always decrease with increasing the distance from the BL. As shown in Fig. 5, our DNS results accord well with the experimental data measured by Wang (red and blue open circles) in the range of $z/\delta$ from 1 to 8 and the DNS results obtained by Wang (green solid circles) for $1 \le z/\delta \le 2$.

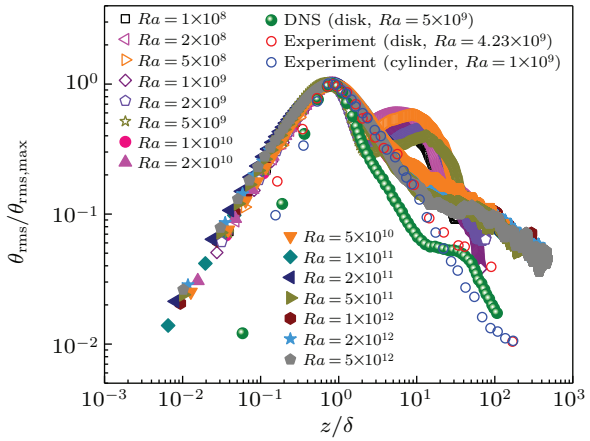



**Fig. 5.** Here data the same as in Fig. 4 but normalized by maximal value $\theta_{\rm rms,max}$ of temperature fluctuations $\theta_{\rm rms}$ where green solid circles and blue empty circles are for thin disk and cylinder, taken from Ref. [21] and red open circles for thin disk taken from Refs. [21,22].

Note that outside 10 BLs, the profiles of the $\theta_{\rm rms}/\theta_{\rm rms,max}$ presented expose some different features from the results acquired Wang, where the temperature fluctuation is found to decrease continuously, probably due to the fact that the effect of corner rolls for their experiments conducted in the thin disk is neglected. However, inside the thermal BL, our data slightly deviate from the experiment data, which may be because there are too few data measured in the boundary layer.

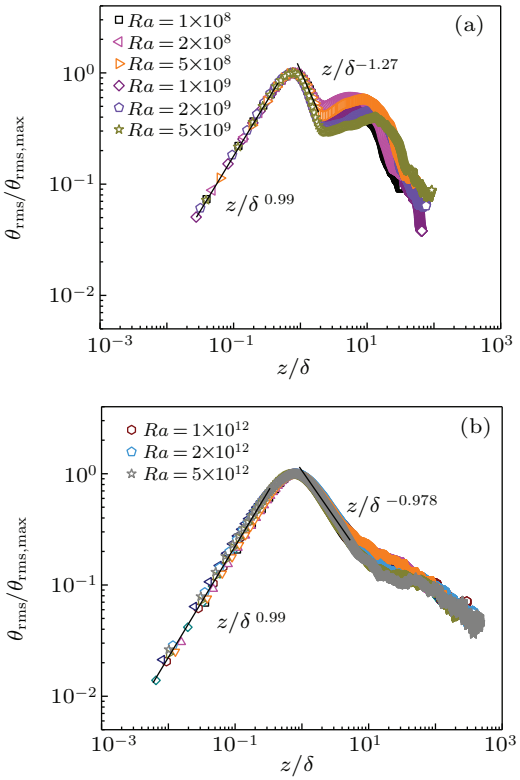



**Fig. 6.** Here data the same as those in Fig. 5, but divided into two plots: (a) from $1.0\times10^8$ to $5.0\times10^9$, (b) from $1.0\times10^{10}$ to $5.0\times10^{12}$, where solid lines show the power-law fits.

To show the temperature fluctuation profiles more clearly, in the following Fig. 6, we plot the same data as those in Fig. 5 but two forms drawn separately corresponding to different values of *Ra*.

Figure 6(a) presents the normalized temperature fluctuation profiles $\theta_{rms}/\theta_{rms,max}$ in the range of *Ra* from $1\times10^8$ to $5\times10^9$. It is seen that the temperature fluctuation $\theta_{rms}/\theta_{rms,max}$ remains unchanged with *Ra* varying and scales with $z/\delta$ in boundary layer, which is in excellent agreement with the previous experimental results.[22,26] The temperature fluctuation $\theta_{rms}/\theta_{rms,max}$ can be well described by the power law, $\theta_{rms}/\theta_{rms,max} \sim (z/\delta)^{0.99}$ with $z/\delta \leq 1$, and $\theta_{rms}/\theta_{rms,max} \sim (z/\delta)^{-1.27}$ in the region $1 \leq z/\delta \leq 2$.

It is seen from Fig. 6(b) that in a wide range of *Ra*, *i.e.*, $Ra \geq 1\times10^{10}$ and these profiles collapse into a single curve irrespective of *Ra*, but there is slight fluctuation in the mixing zone $6 \leq z/\delta \leq 50$. In the boundary layer, the solid line represents a best fit to the data: $\theta_{rms}/\theta_{rms,max} \sim (z/\delta)^{0.99}$, this scaling law is the same as the one in Fig. 5(a). In the region $1 \leq z/\delta \leq 5$, the data can be well described by a power law, *i.e.*, $\theta_{rms}/\theta_{rms,max} \sim (z/\delta)^{-0.978}$ that are consistent with the DNS result[22] for the thin disk.

### 3.3. Global flow features

Regarding the two different characteristics of the temperature fluctuation profiles discussed above, to find the real variation characteristic for the temperature fluctuation, now we come to discuss the temperature and flow characteristics of the system in detail by visualizing the instantaneous temperature fields.

Figure 7 shows the typical example of instantaneous temperature fields at $Pr = 4.3$ with five different values of *Ra*, in which the colormap limit for all temperature snapshots in our study is set between $-0.1 \leq \theta \leq 0.1$, so that the flow structure can be shown clearly. As shown in Figs. 7(a) and 7(b), the overall flow pattern consists of a large clockwise titled-ellipse motion (large-scale circulation) and two corner rolls diagonally opposite to each other. This flow pattern is the same as those observed in previous studies.[38,39] When *Ra* increases to $Ra = 1\times10^{10}$ (Fig. 7(c)), surprisingly, the LSC and two secondary rolls vanish, and the whole flow becomes chaotic. As *Ra* further increases, it is clearly seen from Figs. 7(d) and 7(e) that the flow becomes more chaotic and there are a lot of free cold and hot small vortices. We note that the instantaneous temperature fields before and after $Ra = 1\times10^{10}$ show completely different flow states, suggesting that the mechanism of temperature fluctuation distribution showing two different characteristics may be due to the convective flow change.

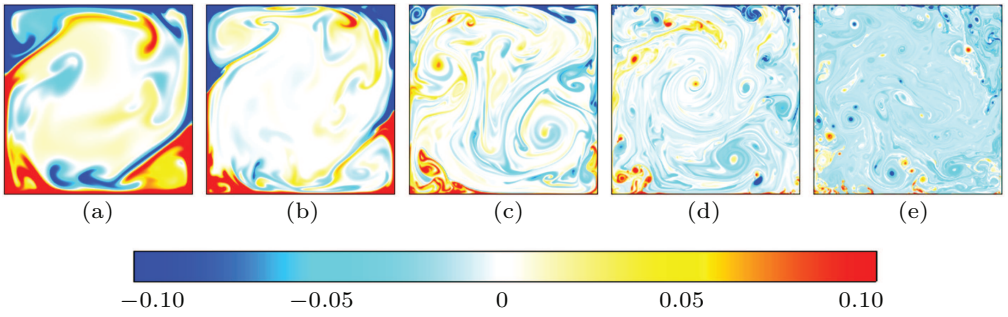



**Fig. 7.** Typical evolution of the instantaneous temperature field with *Ra* at $Pr = 4.3$: (a) $Ra = 1\times10^8$, (b) $Ra = 1\times10^9$, (c) $Ra = 1\times10^{10}$, (d) $Ra = 1\times10^{11}$, (e) $Ra = 1\times10^{12}$.

## 4. Results and discussion for $Pr = 0.7$

The temperature fluctuation and flow structure are discussed in detail for $Pr = 4.3$ above. Next, we will study the temperature fluctuation and flow characteristics with $Pr = 0.7$.

Figure 8(a) shows the variations of temperature fluctuation $\theta_{rms}$ with distance $z/\delta$ from the bottom plate for different

values of $Ra$ and fixed $Pr = 0.7$. It is seen that the temperature fluctuation $\theta_{\rm rms}$ profiles also present two different morphologies. To compare with $Pr = 4.3$, we note that the turning point of the $Ra$ of the two morphologies becomes $Ra = 1 \times 10^9$ and the temperature fluctuation $\theta_{\rm rms}$ does not rise outside the BL. We plot, in Fig. 8(b), the same data as in Fig. 8(a) but $\theta_{\rm rms}$ normalized by maximal value $\theta_{\rm rms,max}$. Inside the BL, all data profiles for different values of $Ra$ always collapse on the top of each other. The solid line represents a power-law fit to the data, $\theta_{\rm rms}/\theta_{\rm rms,max} \sim (z/\delta)^{0.98}$. For $2 < z/\delta < 30$, there are some discrepancies between fluctuation profiles. The temperature fluctuation profiles collapse into a single master curve again when $z/\delta > 30$ for $Ra \geq 1 \times 10^9$.

Figure 9 shows snapshots of the typical temperature field at five different values of $Ra$ for $Pr = 0.7$. It is seen from Fig. 9(a) that the flow consists of large-scale circulation of an ellipse in the bulk and two corner rolls in the upper left and lower right corners. When $Ra$ increases to $Ra = 1 \times 10^9$, the flow structure becomes unexpectedly different, the large-scale circulation of ellipse and two corner rolls disappearing, the convection flows disorderly. Comparing with diverse characteristic of the temperature fluctuation profiles observed in Fig. 8, we find the flow status transition $Ra$ is consistent with the turning point of fluctuation profiles morphology.

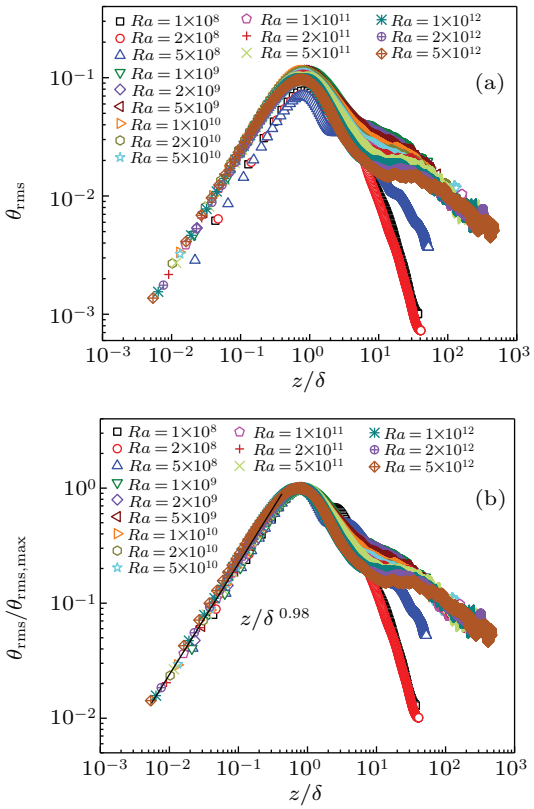



**Fig. 8.** (a) Profiles of temperature fluctuation $\theta_{\rm rms}$ for different values of $Ra$, and (b) normalized $\theta_{\rm rms}/\theta_{\rm rms,max}$ profiles.

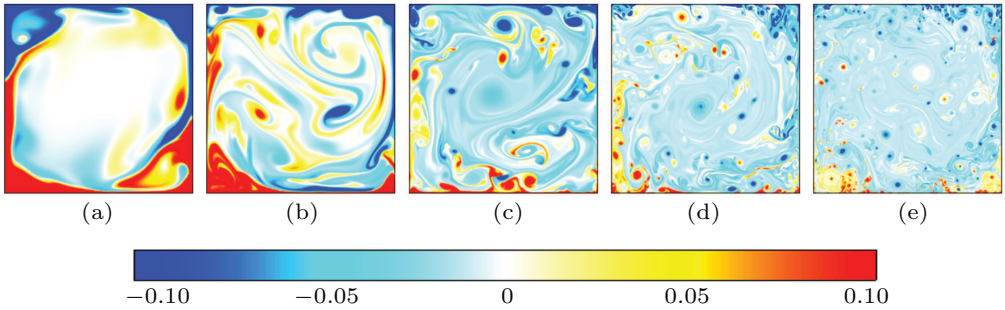



**Fig. 9.** Typical evolution of instantaneous temperature field with $Ra$ at $Pr = 0.7$: (a) $Ra = 1 \times 10^8$, (b) $Ra = 1 \times 10^9$, (c) $Ra = 1 \times 10^{10}$, (d) $Ra = 1 \times 10^{11}$, (e) $Ra = 1 \times 10^{12}$.

The different distribution characteristics of the temperature fluctuation correspond to various flow statuses and plumes' morphologies, and the physical mechanism of the phenomenon correlation will be further discussed.

## 5. The *Ra* dependence of temperature fluctuation properties

Finally, we discuss the $Ra$ dependence of $\langle\theta_{\rm rms}\rangle_V$ for the temperature fluctuation at $Pr = 0.7$ and 4.3, respectively. Here $\langle\cdots\rangle_V$ represents a time average and a spatial average in the black shaded region in Fig. 1(b) (from the bottom plate to the center). Figure 10 show a log–log plot of the temperature fluctuation $\langle\theta_{\rm rms}\rangle_V$ as a function of $Ra$.

It is seen from Fig. 10(a) that the $\langle\theta_{\rm rms}\rangle_V$ *versus* $Ra$ has an apparent transition at $Ra = 1 \times 10^9$. When $Ra$ is below this transition point, there is no obvious characteristic law that describes the relation of $\langle\theta_{\rm rms}\rangle_V$ with $Ra$. At the transition point, $\langle\theta_{\rm rms}\rangle_V$ suddenly increases, then decreases as $Ra$ increases and the change relation between the two quantities is described as $\langle\theta_{\rm rms}\rangle_V \sim Ra^{-0.15\pm0.01}$. Note that the scaling exponent reported here accords well with the previous measurement conducted by Zhou and Xia[35] in a rectangular cell.

Figure 10(b) shows the $\langle\theta_{\rm rms}\rangle_V$ as a function of $Ra$ at $Pr = 4.3$. It can be seen that a similar transition point also exists, which is obviously larger than that at $Pr = 0.7$, i.e., $Ra = 1 \times 10^{10}$. Below the transition point, $\langle\theta_{\rm rms}\rangle_V$ exhibits reduction along with obvious fluctuations. When $Ra$ is beyond this transition point, $\langle\theta_{\rm rms}\rangle_V$ also decreases with $Ra$ increasing and the data can be well described by the power law, $\langle\theta_{\rm rms}\rangle_V \sim (-0.68 \pm 0.01) Ra^{-0.14\pm0.01}$. Interestingly, the ex-

ponent of the power law is the same as the results obtained from experiments.[19,26,31,37]

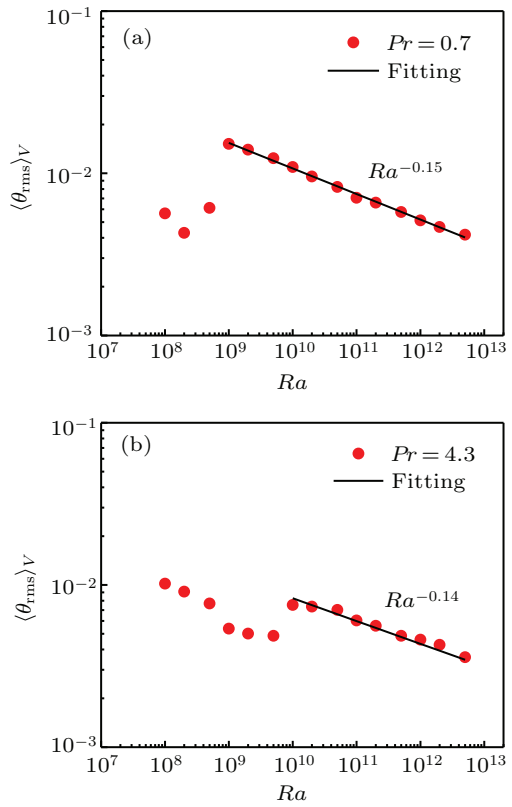



**Fig. 10.** Variations of $\langle\theta_{\rm rms}\rangle_V$ *versus* $Ra$ in central axis range of cell: (a) $Pr = 0.7$, (b) $Pr = 4.3$. The solid lines are power-law fits.

## 6. Conclusions

In this work, we systematically study the statistical properties of the local temperature fluctuation in 2D RBC of aspect ratio unity with the Prandtl number fixed at 0.7 and 4.3 and the Rayleigh number varying from $1 \times 10^8$ to $1 \times 10^{13}$. For the study of temperature fluctuation in the central axis region, we summarize the major findings as follows.

(i) The PDF of the temperature and the temperature fluctuation generally presents a consistent form and can be well described by an exponential function at fixed Prandtl number 4.3 for different values of $Ra$. Integrally, the temperature PDF skews significantly towards higher temperature. The PDF of the temperature fluctuation takes on a symmetrical exponential shape, nevertheless, on the whole it slightly inclines to the right at $Ra = 1 \times 10^{13}$. It is found that the PDF of the temperature and the temperature fluctuation have similar characteristics under each $Ra$.

(ii) With the variation of $Ra$, the profile of temperature fluctuation exhibits two different distribution characteristics at $Pr = 0.7$ and $Pr = 4.3$. When $Pr = 4.3$, in the BL region, all the temperature fluctuation profiles $\theta_{\rm rms}$ collapse into a single master curve. Beyond the boundary layer, the $\theta_{\rm rms}$ profiles decrease with $z/\delta$ increasing, then increase gradually and finally drop dramatically for $Ra < 1 \times 10^{10}$. When $Ra > 1 \times 10^{10}$, the $\theta_{\rm rms}$ profiles continuously decrease and overlap with each other. Normalized fluctuation profiles $\theta_{\rm rms}/\theta_{\rm rms,max}$ also have similar features. Inside the BL, there is a power law, $\theta_{\rm rms}/\theta_{\rm rms,max} \sim (z/\delta)^{0.99}$. Outside the boundary layer, under $Ra \leq 5 \times 10^9$, the $\theta_{\rm rms}/\theta_{\rm rms,max}$ can be described by a power law, $\theta_{\rm rms}/\theta_{\rm rms,max} \sim (z/\delta)^{-1.27}$ with $z/\delta \leq 2$. For $Ra \geq 1 \times 10^{10}$, $\theta_{\rm rms}/\theta_{\rm rms,max} \sim (z/\delta)^{-0.978}$ with $z/\delta \leq 5$. In particular, when $Pr = 0.7$, the temperature fluctuation $\theta_{\rm rms}/\theta_{\rm rms,max}$ profile distribution is similar to that when $Pr = 4.3$. Especially, beyond the temperature boundary layer, the profile always drops and does not upraise. The two different distribution characteristics of temperature fluctuations are closely related to whether there are stable large-scale circulations and corner rolls in the instantaneous flow.

(iii) The $\langle\theta_{\rm rms}\rangle_V$, the spatiotemporal averages of local temperature fluctuation, have similar dependence on $Ra$ for two different $Pr$ numbers. For $Pr = 0.7$, when $Ra$ is above this transition point, *i.e.*, $Ra = 1 \times 10^9$, $\langle\theta_{\rm rms}\rangle_V$ as a function of $Ra$ is well described by the power law $\langle\theta_{\rm rms}\rangle_V \sim Ra^{-0.15\pm0.01}$. While $Pr = 4.3$, the transition point is given by $Ra = 1 \times 10^{10}$. Beyond this transition point, there is also a power law $\langle\theta_{\rm rms}\rangle_V \sim Ra^{-0.14\pm0.01}$.

## Acknowledgements

Project supported by the National Natural Science Foundation of China (Grant No. 11772362), the Shenzhen Fundamental Research Program (Grant No. JCYJ20190807160413162), and the Fundamental Research Funds for the Central Universities, Sun Yat-sen University, China (Grant No. 19lgzd15).

## References

[1] Ahlers G, Grossmann S and Lohse D 2009 *Rev. Mod. Phys.* **81** 503
[2] Lohse D and Xia K Q 2010 *Annu. Rev. Fluid Mech.* **42** 335
[3] Chillà F and Schumacher J 2012 *Eur. Phys. J. E.* **35** 58
[4] Xia K Q 2013 *Theor. Appl. Mech. Lett.* **3** 052001
[5] Grossmann S and Lohse D 2000 *J. Fluid Mech.* **407** 27
[6] Grossmann S and Lohse D 2001 *Phys. Rev. Lett.* **86** 3316
[7] Grossmann S and Lohse D 2002 *Phys. Rev. E* **66** 016305
[8] Krishnamurti R and Howard L N 1981 *Natl. Acad. Sci. USA* **78** 1981
[9] Qiu X L and Tong P 2001 *Phys. Rev. E* **64** 036304
[10] Xia K Q, Sun C and Zhou S Q 2003 *Phys. Rev. E* **68** 066303
[11] Kaminski E and Jaupart C 2003 *J. Fluid Mech.* **478** 287
[12] Zhou Q, Sun C and Xia K Q 2007 *Phys. Rev. Lett.* **98** 074501
[13] van der Poel E P, Verzicco R, Grossmann S and Lohse D 2015 *J. Fluid Mech.* **772** 5
[14] Shang X D, Qiu X L, Tong P and Xia K Q 2003 *Phys. Rev. Lett.* **90** 074501
[15] Shang X D, Tong P and Xia K Q 2008 *Phys. Rev. Lett.* **100** 244503
[16] Gasteuil Y, Shew W L, Gibert M, Chilla F, Castaing B and Pinton J F 2007 *Phys. Rev. Lett.* **99** 234302
[17] Bao Y, He J C and Gao Z Y 2019 *Acta Phys. Sin.* **68** 164701 (in Chinese)
[18] Grossmann S and Lohse D 2004 *Phys. Fluids.* **16** 4462
[19] Castaing B, Gunaratne G, Heslot F, *et al.* 1989 *J. Fluid Mech.* **204** 1

[20] Adrian R J 1996 *Int. J. Heat Mass Transfer* **39** 2303

[21] Wang Y, He X and Tong P 2016 *Phys. Rev. Fluids* **1** 082301

[22] Wang Y, Xu W, He X and Tong P 2018 *J. Fluid Mech.* **840** 408

[23] He Y H and Xia K Q 2019 *Phys. Rev. Lett.* **122** 014503

[24] Deardorff J W 1970 *J. Atmos. Sci.* **27** 1211

[25] Xie Y C, Cheng B Y C, Hu Y B and Xia K Q 2019 *J. Fluid Mech.* **878** R1

[26] Wang J and Xia K Q 2003 *Eur. Phys. J. B* **32** 127

[27] Sun C, Cheung Y H and Xia K Q 2008 *J. Fluid Mech.* **605** 79

[28] Belmonte A, Tilgner A and Libchaber A 1994 *Phys. Rev. E* **50** 269

[29] Fernandes R L J and Adrian R J 2002 *Exp. Therm. Fluid Sci.* **26** 355

[30] Lakkaraju R, Stevens R J A M, Verzicco R, *et al.* 2012 *Phys. Rev. E* **86** 056315

[31] Du Y B and Tong P 2001 *Phys. Rev. E* **63** 046303

[32] Huang S D and Xia K Q 2016 *J. Fluid Mech.* **794** 639

[33] Zhang Y Z, Sun C, Bao Y and Zhou Q 2018 *J. Fluid Mech.* **836** R2

[34] Bao Y, Luo J and Ye M 2018 *J. Mech.* **34** 159

[35] Zhou Q and Xia K Q 2013 *J. Fluid Mech.* **721** 199

[36] Song H and Tong P 2010 *Europhys. Lett.* **90** 44001

[37] Sun C and Xia K Q 2007 *J. Fluid Mech.* **570** 479

[38] Sugiyama K, Ni R, Stevens R J A M, *et al.* 2010 *Phys. Rev. Lett.* **105** 034503

[39] Chandra M and Verma M K 2013 *Phys. Rev. Lett.* **110** 114503